Analysis of Pyrolysis Performance and Molecular Structure of Five Kinds of Low-Rank Coals in Xinjiang Based on the TG-DTG Method

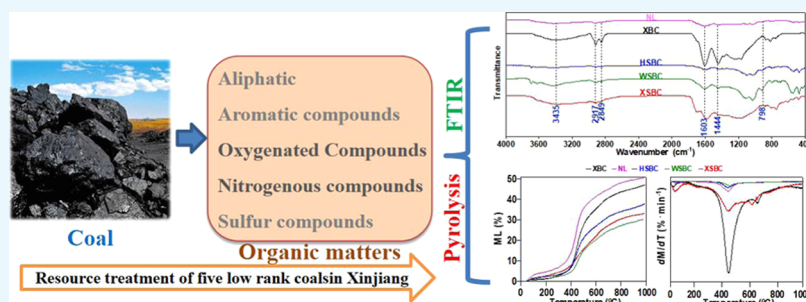Xian-Kang Shan, Shuai-Li Zhao, Ya-Ya Ma, Wenlong Mo,* and Xian-Yong Wei*

Read Online

ACCESS | Metrics & More | Article Recommendations

ABSTRACT: Taking five coal samples (FCSs) in Xinjiang as the research object, characterizations such as proximate analysis, ultimate analysis, Fourier transform infrared (FTIR), and thermogravimetry-differential thermal analysis (TG-DTG) were carried out. The Coats−Redfern model was used to simulate pyrolysis kinetics of FCSs under different reaction orders (ROs). The results showed that except for HSBC, the R^2 of the other four coal samples are all higher than 0.9, which showed a good correlation effect. FCSs present similar reaction activation energy in the same RO and temperature range. Results of FTIR showed that the hydroxyl groups of FCSs, in the range of 3100−3600 cm^{-1}, were mainly self-associated hydroxyl hydrogen bonds and hydroxyl π bonds, and they occupied over 63%. Among them, the pyrolysis characteristic index (D) of XBC was 4.139×10^{-6}, higher than those of other samples, and it showed good pyrolysis performance. Moreover, by reducing the temperature range appropriately, the fitting results showed a better correlation effect.

1. INTRODUCTION

Study of the coal structure is an important foundation for realizing efficient utilization of coal. Studies have shown that the typical chemical structure models of coal included the Fuchs model,[1] Given model,[2] Wiser model,[3] and Shinn model.[4] Because of the complexity of the coal structure and diversity of its properties and utilization, there is still a lack of specific research on coal types with different metamorphisms and coal compositions.[5] The classical physical structural models of coal include the Hirsch model,[6] cross-linking model,[7] host−guest model,[8] association model,[9] and Riley model.[10] Advanced characterization methods such as X-ray diffraction,[11] infrared spectroscopy,[12] nuclear magnetic resonance (NMR) spectroscopy,[13] statistics, and structural analysis[14] have been used in the structural studies of coal.

Pyrolysis of coal is the conversion to organic components of coal by thermal decomposition under anaerobic conditions.[15−17] During this process, decomposition of functional groups (FGs) and fracture of macromolecular chains occur simultaneously.[18] Pyrolysis coke, liquid tar, and pyrolysis gas are the primary products of this process.[19−21] For low-rank coal, more alkyl side chains, heteroatom-containing groups, and higher reaction activity make it easier to realize efficient utilization through pyrolysis conversion.[22,23]

The Coats−Redfern model (CRm) is a commonly used approximation formula, and it is one of the well-known approximate formulas according to previous studies.[24,25] Although its accuracy needs to be improved, CRm is simple to linearize the kinetic equation. More researchers have used it.[26−28] Mo et al.[29] studied the combustion performance for five kinds of oily sludge in Karamay by Fourier transform infrared (FTIR) and thermogravimetry-differential thermal analysis (TG-DTG) analyses, and found that the combustion performance was related to the volatile content. However, many studies[30−32] on pyrolysis/combustion characteristics focused on the combustion part, but there are a few studies on the calculation of the pyrolysis index.

Table 1. Proximate and Ultimate Analyses of FCSs[a]

| sample	proximate analysis, w (%)				ultimate analysis, w (%)					H/C	O/C	LHV[33]	HHV[34]
	M_{ad}	A_d	V_{daf}	FC_{daf}*	C_{daf}	H_{daf}	N_{daf}	$S_{t,d}$	O_{daf}*				
XSBC	16.33	4.00	31.52	68.48	78.46	3.24	0.71	0.40	>17.20	0.50	0.16	22.19	23.37
WSBC	13.32	5.19	32.57	67.42	78.00	3.86	0.93	0.49	>16.73	0.59	0.16	22.56	23.73
HSBC	5.88	21.18	42.81	57.19	74.91	5.65	1.50	0.37	>17.57	0.91	0.18	18.60	19.80
XBC	2.21	3.59	43.86	56.14	78.60	5.27	1.28	0.40	>14.45	0.80	0.14	23.97	25.13
NL	10.36	9.45	52.12	47.88	70.95	3.33	0.63	0.42	>24.67	0.56	0.26	19.07	20.27

[a]*-by difference.
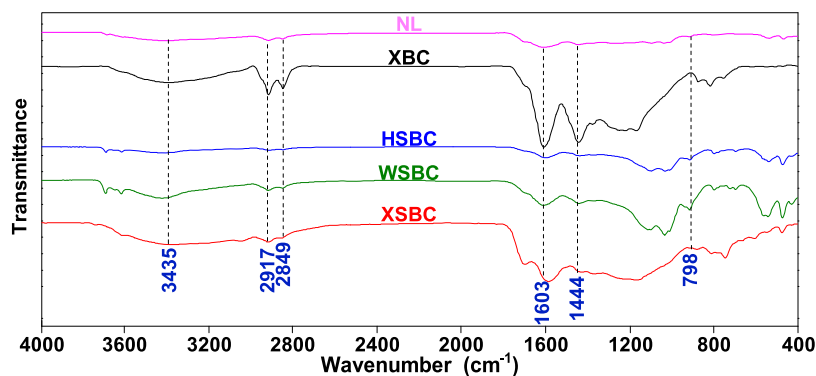
Figure 1. IR distribution of FCSs.

In this paper, five low-rank coals (including lignite, bituminous coal, and sub-bituminous coal) in Xinjiang were taken as the research object. Through FTIR and thermogravimetry tests, the pyrolysis kinetics of FCSs was simulated and analyzed based on the CRm, and the appropriate reaction order (RO) was determined by calculating the fitting parameters. At the same time, the pyrolysis characteristics and pyrolysis index were calculated.

2. RESULTS AND DISCUSSION

2.1. Proximate and Ultimate Analyses. Table 1 shows the proximate and ultimate data of FCSs. As can be seen from Table 1, the moisture (M_{ad}) content of XSBC, NL, and WSBC is above 10%, indicating that they have relatively high M_{ad}. The volatile matter (V_{daf}) of FCSs ranges from 31 to 53%, indicating that the content of small molecules in FCSs varies from region to region and these compounds can be released by pyrolysis. Except for HSBC coal, the ash content (A_d) of the other four samples was very small, below 10%. These studies demonstrate[35,36] that V_{daf} is mainly composed of CO, CO_2, H_2, CH_4, N_2, other small molecular gases, and volatile organic compounds.

Ultimate analysis showed that NL had the least amount of elemental C and XBC had the most, with the amount of elemental H ranging from 3−6%. The O/C ratio of FCSs was relatively low (0.14−0.26), indicating that the organic matter in the FCSs had a high molecular mass and was composed mainly of cyclic compounds.[37,38] The H/C ratio of HSBC was as high as 0.91, which indicates high saturation of organic matter.[39,40]

Furthermore, as can be seen from Table 1, the V_{daf} of FCSs in descending order is as follows: NL > XBC > HSBC > WSBC > XSBC. Since the pyrolysis reaction mainly involves the thermal decomposition of organic matter, so we deduce that the ultimate weight loss (WL) of FCSs is NL > XBC > HSBC > WSBC > XSBC.

2.2. FTIR Analysis. *2.2.1. FTIR Spectrum.* Figure 1 shows the FTIR spectra of FCSs. The absorption peak (Abp) between 3200 and 3600 cm^{-1} is attributed to the hydroxyl group,[41] and Abp at 3435 cm^{-1} is attributed to the OH−π bond. For this FG, XBC, and XSBC are stronger, WSBC is weaker, and the other two coal samples are almost free of this FG. The Abps at 2917 cm^{-1} and 2849 cm^{-1} are attributed to the aliphatic symmetric and asymmetric C−H stretching vibration, such as aliphatic structures −CH_3, −CH_2, and −CH,[42] indicating that there are more aliphatic organic compounds in FCSs. Among them, XBC has the highest strength, followed by XSBC and WSBC, with NL and HSBC with a lower content. The peak at 1603 cm^{-1} belongs to the C=O bond, indicating that FCSs contain ketones, aldehydes, acids, and other substances containing C=O bonds, and here, the Abps of XBC and XSBC are significantly stronger than the other three samples, indicating that they contain relatively more of the three organic compounds mentioned above. At 1444 cm^{-1} is the aromatic ring skeleton vibration Abp, where the order for absorption intensity is XBC < XSBC/WSBC < HSBC < NL, corresponding to the order for the O/C ratio XBC < XSBC/WSBC < HSBC < NL in Table 1. An out-of-plane bending vibration Abp caused by the benzene ring is present in the FCSs at 900−720 cm^{-1}, with the lowest intensity of NL, which is consistent with the weak vibration Abp of the aromatic ring skeleton observed at 1444 cm^{-1}.

2.2.2. FTIR Semiquantitative Analysis. According to the types of FG, the IR spectra can be divided into the following four regions: 3100−3600, 2800−3000, 1000−1800, and 700−900 cm^{-1}.[43,52] The IR spectra of these regions were fitted using Peakfit software and semiquantitative analysis was performed to analyze the FCSs.[44,45,52] The results of the fitting are shown in Figure 2 and Table 2 to provide a detailed understanding of the type and distribution of the organic matter structure in FCSs. The Abp of hydroxyl FGs of FCSs is mainly distributed in the range of 3100−3600 cm^{-1} (Figure 2) and contains
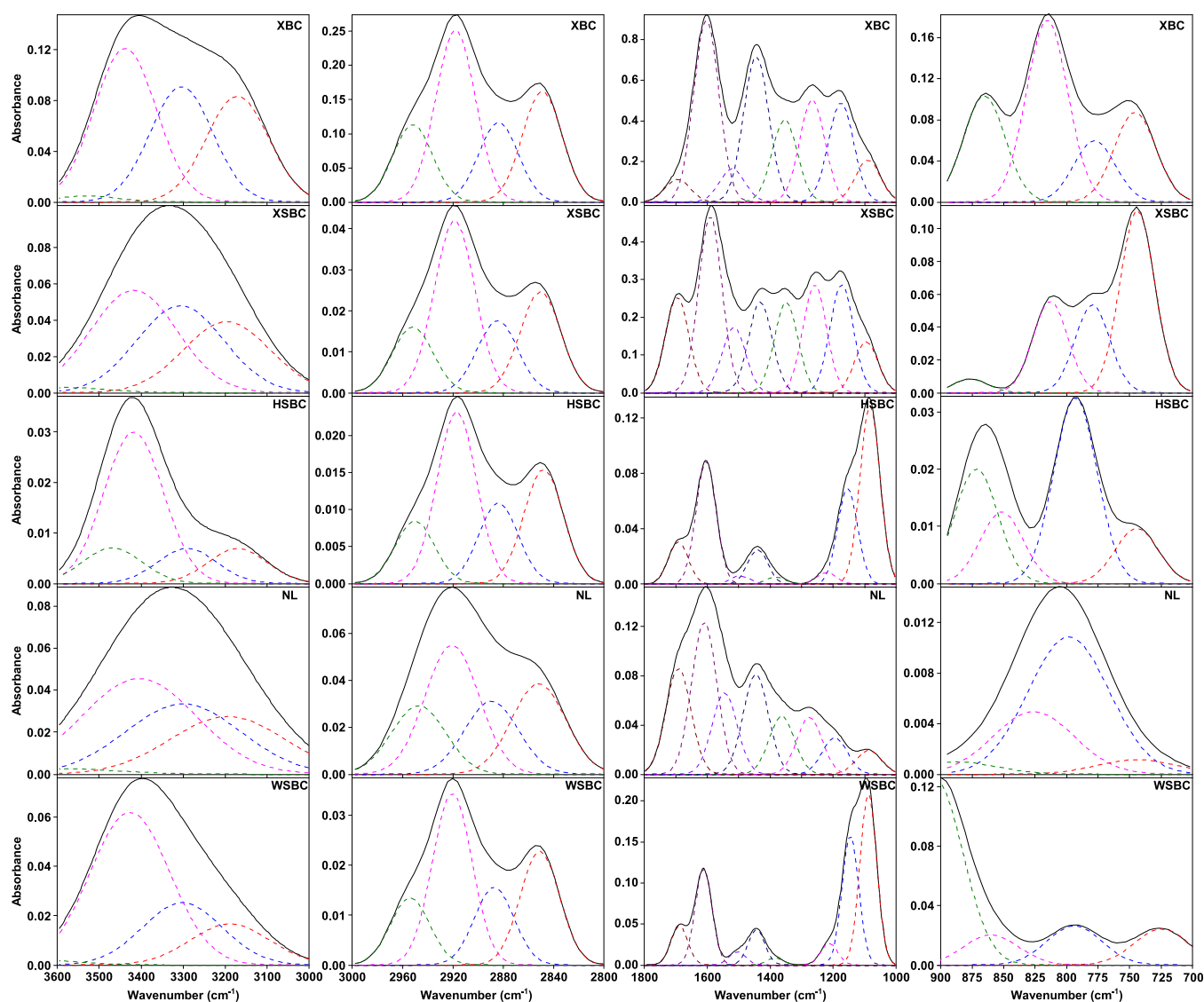
Figure 2. FTIR curve-fitting results of FCSs.

mainly self-associated hydroxyl hydrogen bonds, hydroxyl π bonds, hydroxyl cyclic hydrogen bonds, and hydroxyl ether hydrogen bonds. Within this range, the positions of the IR Abps are almost the same, providing further evidence that the types of FGs in FCSs are the same. In terms of the percentage of the peak area, hydroxyl groups in the FCSs are mainly self-associated hydroxyl hydrogen bonds and hydroxyl π bonds, which account for more than 63% of the total area. Among them, the percentage of self-associated hydroxyl hydrogen bonds was the highest, over 40%.

From Figure 2, aliphatic $-CH_x$ Abps occur in the range of 2800−3000 cm^{-1} with four subpeaks. As can be seen in Table 2, the $-CH_x$ Abp is mainly symmetric and asymmetric aliphatic $-CH_2$, which sum up to approximately 60−70%, with approximately 40% of asymmetric aliphatic $-CH_2$. The other two subpeaks are smaller in area, and the content of aliphatic $-CH$ and aliphatic $-CH_3$ in each component is almost the same, about 19 and 17%, respectively, indicating that aliphatic hydrocarbons in FCSs are mainly in the form of long and less branched chains.[46] As can be seen from Table 2, the FG peak area of FCS varies considerably in the range of 1000−1800 cm^{-1}. The C=O bonds located at 1800−1650 cm^{-1} can be

divided into aliphatic C=O bonds and aromatic C=O bonds. For carboxylic acid C=O appears at 1690 cm^{-1}, NL accounted for 17.21%, and the relative content difference of other samples is very small. Conjugated C=O is found at 1610 cm^{-1}, and the contents of FCSs almost reach more than 20%. There is an aromatic C=C FG at 1560 cm^{-1} with similar content distribution to that at 1690 cm^{-1}. For the FGs at 1350−1245 cm^{-1}, the content of HSBC and WSBC was only about 2.00% and the remaining coal samples contained about 10%. Grease C−O was present at 1090 cm^{-1} in 45.05 and 33.30% for HSBC and WSBC, respectively, while the other three coal samples contained only 5%.

From the peak area data in Table 2, HSBC and NL were mainly trisubstituted by benzene rings in the range of 700−900 cm^{-1}, and their relative contents were 46.04 and 62.38%, respectively; WSBC was mainly substituted by benzene rings with relative contents of 71.53%; XBC was mainly disubstituted by benzene rings with relative contents of 41.67%; and XSBC was mainly tetrasubstituted by benzene rings, and its relative content was 48.65%.

2.3. Pyrolysis Performance of FCSs. *2.3.1. Pyrolysis Characteristics.* Figure 3 shows the TG-DTG curves for FCSs.

Table 2. Change in the Contents of Groups of FCSs

wave number (cm⁻¹)	functional groups	content (%)				
		XSBC	WSBC	HSBC	XBC	NL
3600–3500	OH−π	2.07	0.62	12.05	1.32	1.36
3500–3350	self-associated OH	41.56	58.71	51.27	40.21	41.46
3350–3260	OH−ether O	35.23	24.76	11.87	30.64	32.18
3260–3170	cyclic OH	28.73	15.91	11.77	27.82	25.00
2950	aliphatic −CH_3	15.98	17.91	14.57	17.61	18.90
2920	asymmetric aliphatic −CH_2	41.90	45.79	40.09	39.17	35.83
2890	aliphatic −CH	17.57	20.75	18.77	18.16	20.30
2850	symmetric aliphatic −CH_2	24.54	30.32	26.57	25.06	24.96
1690	carboxylic acids C=O	12.11	7.64	10.69	3.20	17.21
1610	conjugated C=O	22.45	18.79	21.09	25.64	24.73
1560	aromatic C=C	8.37	2.60	2.13	4.69	13.25
1440	asymmetric CH_3−, CH_2−	11.58	6.87	8.77	20.58	16.25
1350	CH_3-Ar, R	11.51	1.36	1.74	11.63	9.45
1245	symmetric deformation −CH_3	13.77	4.26	2.98	14.44	9.30
1165	C−O phenols	13.76	25.15	24.16	14.00	5.95
1090	grease C−O	6.45	33.30	45.05	5.82	3.87
900–860	one adjacent H deformation	3.49	71.53	28.44	23.83	3.56
860–810	two adjacent H deformations	24.41	11.56	17.73	41.67	28.13
810–750	three adjacent H deformations	23.44	15.06	46.04	14.03	62.38
750–720	four adjacent H deformations	48.65	13.86	13.69	20.47	5.92

From the TG diagram, the WL of WSBC is the smallest, about 30.44%; the WL of NL is the largest, about 51.69%; the WL of the other three samples was XSBC, 32.08%; HSBC, 38.77%; and XBC, 47.05% respectively. Based on proximate analysis, WSBC had a V_{daf} of 32.57%; XSBC, HSBC, and XBC had a V_{daf} of 31−44%; and NL had the largest V_{daf} of approximately 50%. Therefore, the higher V_{daf} in the sample, the greater the WL, and slightly higher the WL per sample than V_{daf}. It is possible that the number of samples required for TG characterization is relatively less than for volatility testing. A smaller number of samples transfer more heat, resulting in a higher proportion of substances escaping from coal at the same

temperature. According to the data calculation in Figure 3, the final WL size order of FCSs is NL > XBC > HSBC > XSBC > WSBC. The results are basically consistent with the results in Section 2.1.

As shown in Figure 3, the pyrolysis process of FCSs can be divided into three stages:[47−50] the first stage occurs at around 100 °C. At this stage, water and small molecule gases (N_2, CO_2, CH_4, etc.) will be removed from the coal. The second stage occurs between 400 and 500 °C. At this stage, the pyrolysis reaction is very intense and volatiles are released in the process. The third stage occurs above 550 °C and is mainly a condensation reaction, during which the semi-coke will further decompose and precipitate a large amount of H and a small amount of CH_4. In this stage, the ordering of the semi-coke will be further enhanced and eventually be completely converted into coke.

2.3.2. Conversion−Temperature Relationship. Figure 4 shows the relationship between pyrolysis conversion and
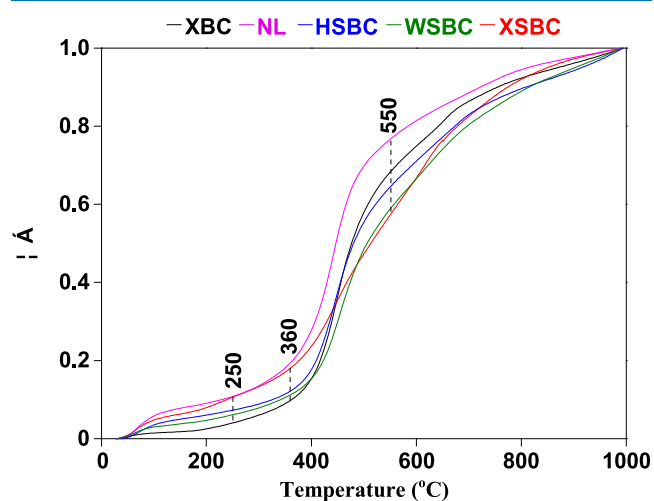
Figure 4. Temperature conversion diagram of FCSs.

temperature. When the CRm is used to perform kinetic fitting of the residue pyrolysis process, we regard it as a complete process for fitting analysis. Because of the significant differences in pyrolysis characteristics at different temperatures, the fitting results have large errors and cannot objectively reflect the pyrolysis of the residue, therefore, the pyrolysis process is divided into three stages of low-temperature, mid-temperature, and high-temperature for kinetic fitting. Combined with the TG-DTG curve and the tangent method,[47,50] we divide the whole process into three temperature ranges:
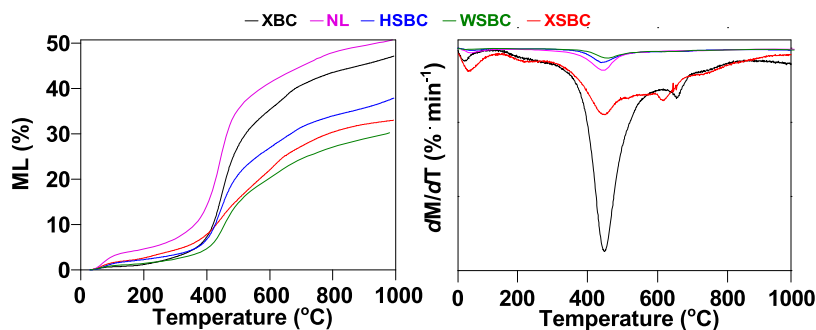
Figure 3. TG-DTG of FCSs.

Table 3. Pyrolysis Characteristics of FCSs[a],

sample	T_i (°C)	T_f (°C)	M_f (%)	M_∞ (%)	T_{max} (°C)	$\Delta T_{1/2}$	WL_1	WL_2	WL_3	D (10^{-7})
XSBC	337.03	701.06	66.99	33.01	445.03	289.47	2.72	27.56	11.36	2.34
WSBC	389.33	612.18	69.56	30.44	458.76	99.27	2.45	12.94	11.48	0.07
HSBC	374.06	579.02	62.12	37.88	440.06	90.01	1.85	19.81	9.53	0.19
XBC	389.33	561.54	52.87	47.13	449.24	86.82	4.35	29.04	9.04	41.39
NL	374.54	533.47	49.31	50.69	439.96	82.22	1.55	14.52	9.17	0.59

[a]The comprehensive pyrolysis characteristic index D extracts to evaluate the pyrolysis characteristics.

Figure 5. Fitting diagram of pyrolysis kinetics of FCSs.

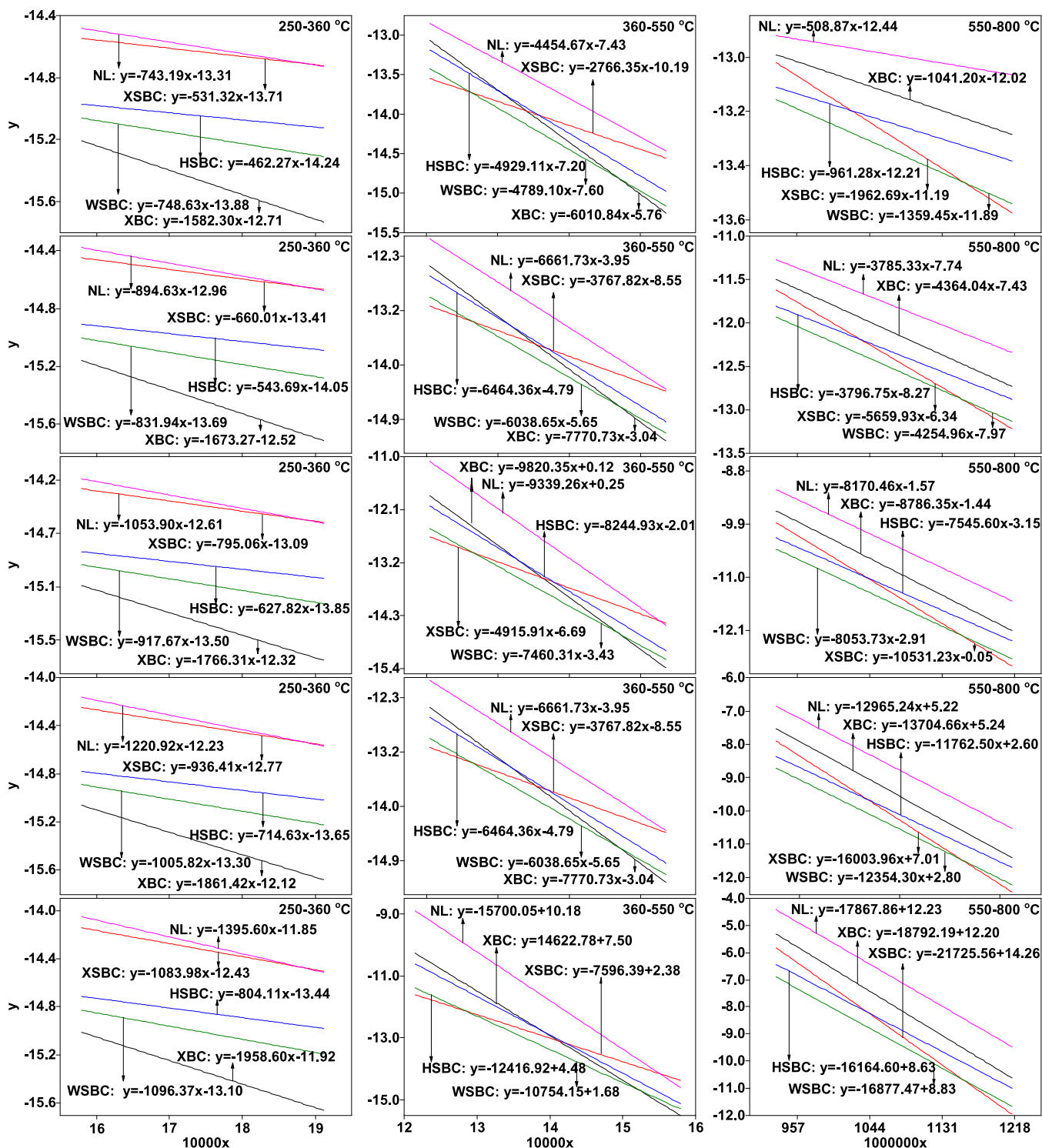**Table 4. Pyrolysis Kinetic Parameters of FCSs with Different Reaction Stages in the Low-Temperature Section**

sample	RO	y	R^2	E (kJ/mol)	A (min^{-1})	2RT/E
			XBC at 250−360 °C			
	1	$-1582.30x - 12.71$	0.9924	13.156	4.79×10^{-2}	0.661
	2	$-1673.27x - 12.52$	0.9914	13.912	6.13×10^{-2}	0.625
	3	$-1766.31x - 12.32$	0.9903	14.686	7.87×10^{-2}	0.592
	4	$-1861.42x - 12.12$	0.9893	15.477	1.01×10^{-1}	0.562
	5	$-1958.60x - 11.92$	0.9882	16.285	1.31×10^{-1}	0.534
			XSBC at 250−360 °C			
	1	$-531.32x - 13.71$	0.9401	4.417	5.92×10^{-3}	1.970
	2	$-660.02x - 13.41$	0.9459	5.488	9.93×10^{-3}	1.585
	3	$-795.06x - 13.09$	0.9495	6.611	1.63×10^{-2}	1.316
	4	$-936.41x - 12.77$	0.9519	7.786	2.66×10^{-2}	1.117
	5	$-1083.98x - 12.43$	0.9535	9.013	4.32×10^{-2}	0.965
			HSBC at 250−360 °C			
	1	$-462.27x - 14.24$	0.8220	3.843	3.02×10^{-3}	2.263
	2	$-543.69x - 14.05$	0.8435	4.520	4.30×10^{-3}	1.924
	3	$-627.82x - 13.85$	0.8591	5.220	6.04×10^{-3}	1.667
	4	$-714.63x - 13.65$	0.8708	5.942	8.42×10^{-3}	1.464
	5	$-804.11x - 13.44$	0.8799	6.686	1.17×10^{-2}	1.301
			NL at 250−360 °C			
	1	$-743.19x - 13.31$	0.9052	6.179	1.24×10^{-2}	1.408
	2	$-894.63x - 12.96$	0.9127	7.438	2.09×10^{-2}	1.170
	3	$-1053.90x - 12.61$	0.9117	8.763	3.53×10^{-2}	0.993
	4	$-1220.92x - 12.23$	0.9212	10.151	5.93×10^{-2}	0.857
	5	$-1395.60x - 11.85$	0.9237	11.604	1.00×10^{-1}	0.750
			WSBC at 250−360 °C			
	1	$-748.63x - 13.88$	0.9532	6.224	7.02×10^{-3}	1.398
	2	$-831.94x - 13.69$	0.9541	6.917	9.42×10^{-3}	1.258
	3	$-917.67x - 13.50$	0.9548	7.630	1.26×10^{-2}	1.140
	4	$-1005.82x - 13.30$	0.9553	8.363	1.68×10^{-2}	1.040
	5	$-1096.37x - 13.10$	0.9556	9.116	2.25×10^{-2}	0.954

low-temperature section (250−360 °C), mid-temperature section (360−550 °C), and high-temperature section (550−800 °C).

Table 3 gives the pyrolysis characteristic indexes of FCSs. According to the literature,[51] the higher the value of D, the better the pyrolysis performance of the sample. The order of D value is XBC > XSBC > NL > HSBC > WSBC, so XBC exhibits best pyrolysis performance, which is 4.139×10^{-6}.

$$D = (\mathrm{d}w/\mathrm{d}t)_{\max} \times (\mathrm{d}w/\mathrm{d}t)_{\mathrm{mean}} \times M_{\infty}$$
$$\times (T_i \times T_{\max} \times \Delta T_{1/2})^{-1}$$

where $(\mathrm{d}w/\mathrm{d}t)_{\max}$ is the maximum mass loss rate (%/min); $(\mathrm{d}w/\mathrm{d}t)_{\mathrm{mean}}$ is the average mass loss rate (%/min), M_{∞} is weight loss, and $M_{\infty} = 1 - M_f/100$ (%); T_i is the initial temperature (°C); $T_{\max}$ is the temperature according to the $(\mathrm{d}w/\mathrm{d}t)_{\max}$, and $\Delta T_{1/2}$ is the temperature interval when $(\mathrm{d}w/\mathrm{d}t)/(\mathrm{d}w/\mathrm{d}t)_{\max} = 0.5$; M_f is the pyrolysis residue mass; ML_1 is the WL in the low-temperature section (250−360 °C); ML_2 is the WL in the mid-temperature section (360−550 °C); and ML_3 is the WL in the high-temperature section (550−800 °C).

In the low and high-temperature sections, the influence of temperature on the pyrolysis conversion is relatively small, and the change of the pyrolysis conversion curve is relatively smooth. In the mid-temperature section, the change of pyrolysis conversion was more obvious as the temperature increased, indicating that more pyrolysis products would be obtained from the decomposition of coal in the mid-

temperature section. Taking n = 1, 2, 3, 4, and 5, the kinetic fitting results are shown in Figure 5 to calculate the kinetic parameters of pyrolysis of FCSs in the low and high-temperature section. The results of the calculations are shown in Tables 4−7.

Table 4 shows the calculated kinetic parameters for the pyrolysis of FCSs at different ROs in the low-temperature section. As can be seen from Table 4 that with the increase of RO, except for HSBC coal, the correlation coefficient R^2 of other coal samples increases, and the value of $R^2 \to 1$, which indicates that the kinetic fitting error gradually decreases. The 2RT/E value decreases with the increase of RO. Combined with the assumption that 2RT/E $\to$ 0 and $R^2 \to 1$, the fitting effect of FCSs is best under n = 5 in the low-temperature section.

In terms of activation energy (AE) at n = 5, HSBC had the lowest AE of 6.686 kJ/mol; XBC and NL had the largest AEs, both above 11 kJ/mol, indicating that HSBC was the most suitable, with the lowest energy consumption for pyrolysis in the low-temperature section at n = 5. Compared to the other samples, XBC and NL had higher energy consumption for pyrolysis and were not suitable for low-temperature pyrolysis.

Table 5 shows the calculated results of the kinetic parameters for the pyrolysis of FCSs at different ROs in the mid-temperature section. As can be seen from Table 5, for n = 1−5, the correlation coefficient R^2 of FCSs has little difference, mainly concentrated above 0.965, indicating that the kinetic fitting errors are small. 2RT/E values decrease with the increase of RO. Combined with the assumption that 2RT/E $\to$

Table 5. Pyrolysis Kinetic Parameters of FCSs with Different Reaction Stages in the Mid-Temperature Section

sample	RO	y	R^2	E (kJ/mol)	A (min^{-1})	2RT/E
			XBC at 360−550 °C			
	1	$-6010.84x - 5.76$	0.9682	49.977	1.89×10^2	0.170
	2	$-7770.73x - 3.04$	0.9795	64.610	3.73×10^3	0.163
	3	$-9820.25x + 0.12$	0.9814	81.651	1.11×10^5	0.129
	4	$-12120.61x + 3.66$	0.9785	100.776	4.71×10^6	0.104
	5	$-14622.78x + 7.50$	0.9737	121.581	3.64×10^8	0.087
			XSBC at 360−550 °C			
	1	$-2766.35x - 10.19$	0.9917	23.001	1.89×10^2	0.458
	2	$-3767.82x - 8.55$	0.9933	31.328	7.27	0.336
	3	$-4915.91x - 6.69$	0.9900	40.873	6.10×10^1	0.258
	4	$-6198.00x - 4.63$	0.9852	51.533	6.07×10^2	0.204
	5	$-7596.39x - 2.38$	0.9804	63.160	7.03×10^3	0.167
			HSBC at 360−550 °C			
	1	$-4929.11x - 7.20$	0.9619	40.983	3.69×10^1	0.257
	2	$-6464.36x - 4.79$	0.9765	53.748	5.84×10^2	0.196
	3	$-8244.93x - 2.01$	0.9815	68.552	1.11×10^4	0.154
	4	$-10241.70x + 1.10$	0.9815	85.155	3.07×10^5	0.124
	5	$-12416.92x + 10.19$	0.9794	103.240	1.09×10^7	0.102
			NL at 360−550 °C			
	1	$-4454.67x - 7.43$	0.9546	37.038	2.63×10^1	0.284
	2	$-6661.72x - 3.95$	0.9739	55.389	1.28×10^3	0.190
	3	$-9339.26x + 0.25$	0.9776	77.651	1.19×10^5	0.136
	4	$-12387.63x + 5.01$	0.9759	102.997	1.86×10^7	0.102
	5	$-15700.15x + 1.68$	0.9731	130.538	4.15×10^8	0.081
			WSBC at 360−550 °C			
	1	$-4789.10x - 7.60$	0.9732	39.819	2.39×10^2	0.264
	2	$-6038.65x - 5.65$	0.9762	50.208	214×10^2	0.210
	3	$-7460.31x - 3.43$	0.9743	62.029	2.12×10^4	0.170
	4	$-9039.07x - 0.98$	0.9700	75.155	3.39×10^4	0.141
	5	$-10754.15x + 1.68$	0.9650	89.415	5.76×10^8	0.118

0, the results indicate that the reaction model is more suitable for the pyrolysis process as RO increases. Considering that the fitted correlation coefficient R^2 is similar, the lower the RO, the lower the AE. Therefore, the fitting effect of FCSs is best when $n = 1$ in the mid-temperature section.

From the AE values for $n = 1$, XSBC had the smallest AE value of 31.328 kJ/mol; XBC and NL had the largest AE, both above 121 kJ/mol, indicating that XSBC was the most suitable and had the lowest energy consumption for pyrolysis in the mid-temperature section and $n = 1$, while XBC and NL were not suitable in this temperature range.

Table 6 shows the calculated kinetic parameters for the pyrolysis of FCSs in different reaction stages in the high-temperature section. From Table 6, it can be seen that the correlation coefficient R^2 values gradually decreased with the increase of RO, except for XBC and NL, indicating that the kinetic fitting error gradually increased. 2RT/E values decreased with the increase of RO, combined with the assumption that 2RT/E → 0, it shows that with the increase of the RO, the reaction model is more suitable for the pyrolysis process, and combined with the assumption that R^2 → 1, $n = 2$ is more suitable for the high-temperature section. In terms of AE at $n = 2$, WSBC had the smallest AE of 25.378 kJ/mol and the XSBC coal sample had the largest AE of 47.060 kJ/mol, indicating that WSBC was the most suitable and had the lowest energy consumption for pyrolysis in the high-temperature section and at $n = 2$, and XSBC coal sample was the opposite.

From Tables 4 to 6, in the low-temperature section, 2RT/E values decrease with the increase of RO for the other four coal samples except for XBC; however, the correlation coefficient R^2 decreases significantly with the increase of RO, indicating an increasingly poor fit to the pyrolysis kinetics. From the AE data, it can be found that AE increases with the increasing number of RO. Considering 2RT/E → 0 and kinetic fitting, the pyrolysis RO of the above FCSs in the low-temperature section is considered to be 5.

In the mid-temperature section, the FCSs correlation coefficient R^2 is similar and the kinetic fitting errors are small. 2RT/E values decrease with the increasing number of RO. Considering the AE of the reaction, the energy consumption is lower when $n = 1$.

In the high-temperature section, the 2RT/E values of FCSs decrease with increasing number of RO, but when RO $n = 1$, the 2RT/E values were relatively large, some even greater than 1, which was inconsistent with the assumption that 2RT/E → 0, indicating that CRm was not applicable at this temperature. At RO of 2, 3, 4, and 5, the correlation coefficient R^2 → 1, indicates a good fit for the kinetics of coal pyrolysis; the results show that the pyrolysis of FCSs at high-temperature is dominated by $n = 2$, 3, 4, and 5.

2.3.3. Comparative Analysis. It is worth mentioning that when calculating the kinetic parameters of the low-temperature section, the correlation coefficient is different because of the division of different temperature sections. Therefore, this paper simply analyzed the influence of different temperature sections on the correlation coefficient in the low-temperature section.

Table 6. Pyrolysis Kinetic Parameters of FCSs with Different Reaction Stages in the High-Temperature Section

sample	RO	y	R^2	E (kJ/mol)	A (min^{-1})	2RT/E
			XBC at 550−800 °C			
	1	$-1041.20x + 12.02$	0.9796	8.657	6.27×10^{-2}	1.581
	2	$-4364.04x - 7.43$	0.9932	36.285	2.58×10^{1}	0.377
	3	$-8786.35x - 1.44$	0.9896	73.054	2.09×10^{4}	0.187
	4	$-13704.66x + 5.24$	0.9887	113.947	2.60×10^{7}	0.120
	5	$-18792.20x + 12.20$	0.9887	156.247	3.73×10^{10}	0.088
			XSBC at 550−800 °C			
	1	$-964.58x + 11.19$	0.9991	16.319	2.71×10^{-1}	0.839
	2	$-5659.93x - 6.34$	0.9915	47.060	9.95×10^{1}	0.291
	3	$-10531.23x - 0.05$	0.9833	87.562	9.99×10^{4}	0.156
	4	$-16003.96x + 7.01$	0.9803	133.064	1.78×10^{8}	0.103
	5	$-21725.56x + 14.43$	0.9796	180.637	4×10^{11}	0.076
			HSBC at 550−800 °C			
	1	$-961.58x - 12.21$	0.9817	7.995	4.77×10^{2}	1.712
	2	$-3796.75x - 8.27$	0.9935	31.568	9.73	0.434
	3	$-7545.60x - 0.05$	0.9897	62.738	3.22×10^{3}	0.218
	4	$-11762.50x + 2.60$	0.9885	97.799	1.58×10^{6}	0.140
	5	$-16164.60x + 8.63$	0.9883	134.400	9.05×10^{8}	0.102
			NL at 550−800 °C			
	1	$-508.87x - 12.45$	0.9012	4.231	2.00×10^{-2}	3.24
	2	$-3785.33x - 7.74$	0.9499	31.473	1.64×10^{1}	0.435
	3	$-8170.46x - 1.57$	0.9529	67.933	1.7×10^{4}	0.201
	4	$-12965.24x + 5.22$	0.9557	107.799	2.41×10^{7}	0.127
	5	$-17867.86x + 12.23$	0.9843	148.562	3.67×10^{10}	0.092
			WSBC at 550−800 °C			
	1	$-1359.45x - 11.89$	0.9945	11.303	9.33×10^{2}	1.211
	2	$-4254.96x + 14.43$	0.9935	25.378	1.48×10^{1}	0.387
	3	$-8053.73x - 2.91$	0.9872	66.962	4.37×10^{3}	0.204
	4	$-12354.30x + 2.797$	0.9849	102.720	2.03×10^{6}	0.133
	5	$-16877.47x + 8.826$	0.9843	140.327	1.15×10^{9}	0.098

Table 7 shows the calculated pyrolysis kinetic parameters for FCSs with different ROs in the original low-temperature section (170−360 °C). As can be seen from Table 6, the R^2 is as low as 0.4587 and 0.4781 for HSBC and NL, respectively, which showed poor correlation. To solve this problem, we adjusted the original temperature section (170−360 °C) to a new one (250−360 °C) and the problem was effectively solved. The maximum R^2 for HSBC and NL increased to 0.8708 and 0.9237, respectively, and the fitted results showed good correlations. Therefore, we speculate that the differences in pyrolysis characteristics between the above two coal samples in the original temperature range are too large, resulting in large errors in the fitting results when fitting the kinetics of the coal pyrolysis process with the CRm model, which cannot objectively reflect the pyrolysis of coal samples. Therefore, on appropriately reducing the temperature range, the fitted results showed a better correlation.

temperature and $n = 1$, HSBC was the most suitable and had the lowest pyrolysis energy consumption. The pyrolysis energy consumption of XBC and NL coal samples is large. In the mid-temperature section and at $n = 1$, XSBC was the most suitable and had the lowest pyrolysis energy consumption. XBC and NL had higher pyrolysis energy consumption. In the high-temperature section, $n = 2$, WSBC is the most suitable and has the lowest pyrolysis energy consumption. XSBC has a higher pyrolysis energy consumption. Through the kinetic fit plots of FCSs and RO, it is found that with the increase of RO, the higher the temperature, the more obvious the effect of temperature on the conversion rate. When fitting the kinetics of the pyrolysis process of FCSs with CRm, the fitting results have large errors and could not objectively reflect the pyrolysis process of FCSs. Therefore, by appropriately reducing the temperature range, the fitted results showed a better correlation.

3. CONCLUSIONS

The IR spectra showed that in the range of 3600−3100 cm^{-1}, the hydroxyl groups in FCSs are mainly self-associating hydroxyl hydrogen bond, hydroxyl hydrogen bond, and hydroxyl cyclic hydrogen bond; in the range of 2800−3000 cm^{-1}, the Abps of FCSs are mainly symmetric and asymmetric aliphatic −CH$_2$; in the range of 1000−1800 cm^{-1}, conjugated C=O is found at 1610 cm^{-1}. By calculating the pyrolysis characteristic index, XBC was found to have better pyrolysis performance. TG-DTG showed that the FCSs showed good correlation at low, medium, and high temperatures; at low-

4. EXPERIMENTAL SECTION

4.1. Raw Materials. The raw materials used in this experiment are Xigou bituminous coal (XBC), Xiheishan sub-bituminous coal (XSBC), Hefeng sub-bituminous coal (HSBC), Naomaohu lignite (NL), and Wucaiwan sub-bituminous coal (WSBC) from Xinjiang (China). The sample preparation method is ASTM D2013-2007. Before the experiment, the coal samples were ground and passed through a 200 mesh sieve.

4.2. Analysis Methods. Proximate analysis, ultimate analysis, FTIR, and TG-DTG characterization studies were

Table 7. Pyrolysis Kinetic Parameters of FCSs with Different ROs in the Original Low-Temperature Section (170−360 °C)

sample	RO	y	R^2	E (kJ/mol)	A (min^{-1})	2RT/E
			XBC at 170−360 °C			
	1	$-1402.64x - 13.02$	0.9917	11.662	3.11×10^{-2}	0.632
	2	$-1461.34x - 12.88$	0.9902	12.150	3.71×10^{-2}	0.606
	3	$-1521.10x - 12.74$	0.9887	12.647	4.44×10^{-2}	0.583
	4	$-1581.91x + 12.60$	0.9871	13.153	5.31×10^{-2}	0.560
	5	$-1643.78x - 12.46$	0.9855	13.667	6.4×10^{-2}	0.539
			XSBC at 170−360 °C			
	1	$-459.80x - 13.83$	0.9776	3.823	3.12×10^{4}	1.928
	2	$-552.54x - 13.59$	0.9754	4.594	7×10^{-3}	1.604
	3	$-649.10x - 12.74$	0.9730	5.397	1×10^{-2}	1.365
	4	$-749.48x - 13.09$	0.9706	6.232	1.5×10^{-2}	1.183
	5	$-853.64x - 12.83$	0.9682	7.098	2.3×10^{-2}	1.038
			HSBC at 170−360 °C			
	1	$-158.13x - 14.76$	0.4587	1.315	6.12×10^{-4}	5.605
	2	$-210.21x - 14.62$	0.5595	1.748	9.37×10^{-4}	4.216
	3	$-263.78x - 14.48$	0.6289	2.193	1.36×10^{-3}	3.360
	4	$-318.86x - 14.33$	0.6781	2.651	1.90×10^{-3}	2.780
	5	$-375.43x - 14.18$	0.7141	3.122	2.61×10^{-3}	2.361
			NL at 170−360 °C			
	1	$-256.18x - 14.14$	0.4781	2.130	1.84×10^{-3}	3.460
	2	$-345.46x - 13.91$	0.5709	2.872	3×10^{-3}	2.566
	3	$-438.78x - 113.67$	0.6327	3.648	5×10^{-3}	2.020
	4	$-536.12x - 13.41$	0.6755	4.458	8×10^{-3}	1.653
	5	$-637.43x - 13.15$	0.7064	5.300	1.2×10^{-2}	1.390
			WSBC at 170−360 °C			
	1	$-1539.11x + 0.21$	0.9827	4.015	1.91×10^{4}	1.835
	2	$-482.88x - 14.34$	0.9085	4.470	2.87×10^{-3}	1.648
	3	$-593.81x - 14.06$	0.9113	4.937	5×10^{-3}	1.493
	4	$-651.29x - 13.91$	0.9122	5.415	6×10^{-3}	1.361
	5	$-710.11x - 13.76$	0.9127	5.904	7×10^{-3}	1.248

carried out on five coal samples (FCSs). A GB/T 28731-2012 was used for proximate analysis, a VarioMax elemental analyzer was used for ultimate analysis, FTIR was performed using a TENSOR-27 infrared spectrometer, and TG-DTG was performed using a SDT Q600 thermogravimetric analyzer and the system was heated from 298 K to 1253 K at a rate of 5 K/min with N_2 as the carrier gas.

4.3. Kinetics Study. CRm[52−54] was used to simulate the pyrolysis kinetics of FCSs and the method of CRm can refer to the previous work of Mo et al.[52]

■ AUTHOR INFORMATION

Corresponding Authors

Wenlong Mo − State Key Laboratory of Chemistry and Utilization of Carbon-Based Energy Resources and Key Laboratory of Coal Clean Conversion & Chemical Engineering Process (Xinjiang Uyghur Autonomous Region), College of Chemical Engineering, Xinjiang University, Ürümqi, Xinjiang 830046, China; orcid.org/0000-0003-3837-0915; Phone: 15022994903; Email: mowenlong@xju.edu.cn

Xian-Yong Wei − State Key Laboratory of Chemistry and Utilization of Carbon-Based Energy Resources and Key Laboratory of Coal Clean Conversion & Chemical Engineering Process (Xinjiang Uyghur Autonomous Region), College of Chemical Engineering, Xinjiang University, Ürümqi, Xinjiang 830046, China; Jiangsu Province Engineering Research Center of Fine Utilization of Carbon Resources, China University of Mining and Technology, Xuzhou, Jiangsu 221116, China; orcid.org/0000-0001-7106-4624; Phone: 13641538902; Email: wei_xianyong@163.com

Authors

Xian-Kang Shan − State Key Laboratory of Chemistry and Utilization of Carbon-Based Energy Resources and Key Laboratory of Coal Clean Conversion & Chemical Engineering Process (Xinjiang Uyghur Autonomous Region), College of Chemical Engineering, Xinjiang University, Ürümqi, Xinjiang 830046, China

Shuai-Li Zhao − State Key Laboratory of Chemistry and Utilization of Carbon-Based Energy Resources and Key Laboratory of Coal Clean Conversion & Chemical Engineering Process (Xinjiang Uyghur Autonomous Region), College of Chemical Engineering, Xinjiang University, Ürümqi, Xinjiang 830046, China

Ya-Ya Ma − State Key Laboratory of Chemistry and Utilization of Carbon-Based Energy Resources and Key Laboratory of Coal Clean Conversion & Chemical Engineering Process (Xinjiang Uyghur Autonomous Region), College of Chemical Engineering, Xinjiang University, Ürümqi, Xinjiang 830046, China

Notes

The authors declare no competing financial interest.

■ REFERENCES

(1) Yang, Y. H.; Pan, J. N.; Wang, K.; Hou, Q. L. Macromolecular structural response of Wender coal under tensile stress via molecular dynamics. *Fuel* **2020**, *265*, No. 116938.

(2) Li, L.; Fan, H. J.; Hu, H. Q. Distribution of hydroxyl group in coal structure: A theoretical investigation. *Fuel* **2017**, *189*, 195−202.

(3) Wang, H. J.; Feng, Y. H.; Zhang, X. X.; Lin, W.; Zhao, Y. L. Study of coal hydropyrolysis and desulfurization by ReaxFF molecular dynamics simulation. *Fuel* **2015**, *145*, 241−248.

(4) Hong, D. K.; Liu, L.; Wang, C. B.; Si, T.; Guo, X. Construction of a coal char model and its combustion and gasification characteristics: Molecular dynamic simulations based on ReaxFF. *Fuel* **2021**, *300*, No. 120972.

(5) Smirnov, V. G.; Dyrdin, V. V.; Manakov, A. Y.; Fedorova, N. I.; Shikina, N. V.; Ismagilov, Z. R. Physicochemical and Sorption Properties of Natural Coal Samples with Various Degrees of Metamorphism. *Russ. J. Appl. Chem.* **2019**, *92*, 1410−1421.

(6) Wu, D.; Zhang, W. Y.; Krafft, C. Evolution Mechanism of Macromolecular Structure in Coal during Heat Treatment: Based on FTIR and XRD In Situ Analysis Techniques. *J. Spectrosc.* **2019**, No. 5037836.

(7) Qiang, L. Y.; Bai, B. Y.; Peng, Z. W.; Zhang, S. S.; Chang, H.; Sun, M.; Xu, L.; Ma, X. X. Research on the relationship between the structure and pyrolysis characteristics of pretreated Shendong coal. *Fuel* **2021**, *305*, No. 121515.

(8) Zou, L.; Jin, L. J.; Li, Y.; Zhu, S. W.; Hu, H. Q. Effect of tetrahydrofuran extraction on lignite pyrolysis under nitrogen. *J. Anal. Appl. Pyrolysis* **2015**, *112*, 113−120.

(9) Du, J. T.; Zhang, D. K.; Zhang, M. X.; Jia, H. N.; Nie, Y.; Sun, Y. K.; Deng, W. A.; LI, C. Structure characteristics and association behavior of coal and petroleum C7-asphaltenes. *J. Fuel Chem. Technol.* **2020**, *48*, 674−682.

(10) Vejahati, F.; Xu, Z. H.; Gupta, R. Trace elements in coal: Associations with coal and minerals and their behavior during coal utilization − A review. *Fuel* **2010**, *89*, 904−911.

(11) Li, Q. Z.; Tao, Q. L.; Yuan, C. C.; Zheng, Y. N.; Zhang, G. Y.; Liu, J. F. Investigation on the structure evolution of pre and post explosion of coal dust using X-ray diffraction. *Int. J. Heat Mass Transfer* **2018**, *120*, 1162−1172.

(12) Yin, Y. S.; Yin, H. X.; Wu, Z. H.; Qi, C. W.; Tian, H.; Zhang, W.; Hu, Z. M.; Feng, L. H. Characterization of Coals and Coal Ashes with High Si Content Using Combined Second-Derivative Infrared Spectroscopy and Raman Spectroscopy. *Crystals* **2019**, *9*, No. 513.

(13) Mao, Y. Q.; Xia, W. C.; Xie, G. Y.; Peng, Y. L. Rapid detection of the total moisture content of coal fine by low-field nuclear magnetic resonance. *Measurement* **2020**, *155*, No. 107564.

(14) Kursunoglu, N.; Onder, M. Technology - Underground Space Technology; Reports on Underground Space Technology Findings from Eskisehir Osmangazi University Provide New Insights (Application of Structural Equation Modeling To Evaluate Coal and Gas Outbursts). *J. Technol.* **2019**, *88*, 63−72.

(15) Zhou, Y.; Li, L.; Jin, L. J.; Zhu, J. L.; Li, J. G.; Li, Y.; Fan, H. J.; Hu, H. Q. Effect of functional groups on volatile evolution in coal pyrolysis process with in-situ pyrolysis photoionization time-of-flight mass spectrometry. *Fuel* **2020**, *260*, No. 116322.

(16) Yi, L.; Feng, J.; Li, W. Y. Evaluation on a combined model for low-rank coal pyrolysis. *Energy* **2019**, *169*, 1012−1021.

(17) Hong, D. K.; Guo, X. Molecular dynamics simulations of Zhundong coal pyrolysis using reactive force field. *Fuel* **2017**, *210*, 58−66.

(18) Xin, F. D.; Xu, H.; Tang, D. Z.; Yang, J. S.; Chen, Y. P.; Cao, L. K.; Qu, H. X. Pore structure evolution of low-rank coal in China. *Int. J. Coal Geol.* **2019**, *205*, 126−139.

(19) Lei, Z.; Shu, H.; Jia, Y.; Zhang, L.; Xu, D. Study on solid waste pyrolysis coke catalyst for catalytic cracking of coal tar. *Int. J. Hydrogen Energy* **2020**, *45*, 19280−19290.

(20) Pan, D. F.; Qu, X.; Bi, J. C. Effect of gasified semi-coke on coal pyrolysis in the poly-generation of CFB gasification combined with coal pyrolysis. *J. Anal. Appl. Pyrolysis* **2017**, *127*, 461−467.

(21) Yu, W. H.; Han, S.; Lei, Z. P.; Zhang, K.; Yan, J. C.; Li, Z. K.; Shui, H. F.; Kang, S. G.; Wang, Z. C.; Ren, S. B.; Pan, C. X. The reaction behavior of volatiles generated from lignite pyrolysis. *Fuel* **2019**, *244*, 22−30.

(22) Xu, T.; Pisupati, S. V.; Bhattacharya, S. Comparison of entrained flow CO_2 gasification behaviour of three low-rank coals − Victorian brown coal, Beulah lignite, and Inner Mongolia lignite. *Fuel* **2019**, *249*, 206−218.

(23) Tian, H. Y.; Pan, J.; Zhu, D. Q.; Guo, Z. Q.; Yang, C. C.; Xue, Y. X.; Li, S. W.; Wang, Y. Y. Innovative one-step preparation of activated carbon from low-rank coals activated with oxidized pellets. *J. Cleaner Prod.* **2021**, *313*, No. 127877.

(24) Naqvi, S. R.; Tariq, R.; Hameed, Z.; Ali, I.; Naqvi, M.; Chen, W. H.; Ceylan, S.; Rashid, H.; Ahmad, J.; Taqvi, S.; Shahbaz, M. Pyrolysis of high ash sewage sludge: Kinetics and thermodynamic analysis using Coats-Redfern method. *Renewable Energy* **2019**, *131*, 854−860.

(25) Mian, I.; Li, X.; Jian, Y. M.; Dacres, O. D.; Zhong, M.; Liu, J. M.; Ma, F. Y.; Rahman, N. Kinetic study of biomass pellet pyrolysis by using distributed activation energy model and Coats Redfern methods and their comparison. *Bioresour. Technol.* **2019**, *294*, No. 122099.

(26) Song, F. H.; Wang, X. J.; Li, T. T.; Zhang, J.; Bai, Y. C.; Xing, B. S.; Giesy, J. P.; Wu, F. C. Spectroscopic analyses combined with Gaussian and Coats-Redfern models to investigate the characteristics and pyrolysis kinetics of sugarcane residue-derived biochars. *J. Cleaner Prod.* **2019**, *237*, No. 117855.

(27) Surahmanto, F.; Harwin, S.; Hary, S.; Tri, A. R. Investigation of the pyrolysis characteristics and kinetics of oil-palm solid waste by using Coats−Redfern method. *Energy Explor. Exploit.* **2020**, *38*, 298−309.

(28) Li, J. J.; Dou, B. L.; Zhang, H.; Zhang, H.; Chen, H. S.; Xu, Y. J. Thermochemical characteristics and non-isothermal kinetics of camphor biomass waste. *J. Environ. Chem. Eng.* **2021**, *9*, No. 105311.

(29) Mo, W. L.; Shan, X. K.; He, X. Q.; Qiang, W. J.; Wei, X. Y.; Wei, B.; Fan, X.; Wu, Y. L. Functional group characteristics and pyrolysis/combustion performance of Karamay OS based on FT-IR and TG−DTG analyses. *ACS Omega* **2021**, *6*, 27684−27696.

(30) Jayaraman, K.; Mustafa, V. K.; Iskender, G. Combustion mechanism and model free kinetics of different origin coal samples: Thermal analysis approach. *Energy* **2020**, *204*, No. 117905.

(31) Jayaraman, K.; Mustafa, V. K.; Iskender, G. Thermogravimetric and mass spectrometric (TG-MS) analysis and kinetics of coal-biomass blends. *Renewable Energy* **2017**, *101*, 293−300.

(32) Jayaraman, K.; Mustafa, V. K.; Iskender, G. Pyrolysis, combustion and gasification studies of different sized coal particles using TGA-MS. *Appl. Therm. Eng.* **2017**, *125*, 1446−1455.

(33) Drudi, K. C. R.; Ricardo, D.; Gilberto, M.; Graziella, C.; Antonio, J. T. C. L. Statistical model for heating value of municipal solid waste in Brazil based on gravimetric composition. *Waste Manage.* **2019**, *87*, 782−790.

(34) Parikh, J.; Channiwala, S.; Ghosal, G. A correlation for calculating HHV from proximate analysis of solid fuels. *Fuel* **2005**, *84*, 487−494.

(35) Yan, C.; Qi, J.; Liang, J.; et al. Determination of coal properties using laser-induced breakdown spectroscopy combined with kernel extreme learning machine and variable selection. *J. Anal. At. Spectrom.* **2018**, *33*, 2089−2097.

(36) Liu, W.; Ouyang, Z.; Cao, X.; Na, Y. The influence of air-stage method on flameless combustion of coal gasification fly ash with coal self-preheating technology. *Fuel* **2019**, *235*, 1368−1376.

(37) Ugo, M.; Federico, B.; Felix, K. Formation of highly oxygenated organic molecules from aromatic compounds. *Atmos. Chem. Phys.* **2018**, *18*, 1909−1921.

(38) Jeguirim; Mejdi; Haddad. New insights on the structural evolution of biomass char upon pyrolysis as revealed by the Raman spectroscopy and elemental analysis. *Carbon* **2017**, *119*, 519−521.

(39) Pang, Y.; Lu, Y.; Wang, X.; et al. Computational estimation on the propulsion performance of polycyclic hydrocarbons. *Chem. Eng. Sci.* **2021**, *246*, No. 117010.

(40) Zhao, H.; Li, Y.; Song, Q.; et al. Investigation on the thermal behavior characteristics and products composition of four pulverized coals: Its potential applications in coal cleaning. *Int. J. Hydrogen Energy* **2019**, *44*, 23620−23638.

(41) Zhang, Y.; Zhao, H.; Shi, Q.; Chung, K. H.; Zhao, S.; Xu, C. Molecular investigation of crude oil sludge from an electric dehydrator. *Energy Fuels* **2011**, *25*, 3116−3124.

(42) Zhu, X.; Yang, S.; Wang, L.; Liu, Y.; Qian, F.; Yao, W.; et al. Tracking the conversion of nitrogen during pyrolysis of antibiotic mycelial fermentation residues using XPS and TG-FTIR-MS technology. *Environ. Pollut.* **2016**, *211*, 20−7.

(43) Ma, Y. Y.; Ma, F. Y.; Mo, W. L.; Wang, Q. Five-stage sequential extraction of Hefeng coal and direct liquefaction performance of the extraction residue. *Fuel* **2020**, *266*, 117039−117048.

(44) Wang, S. Q.; Tang, Y. G.; Schobert, H. H.; Guo, Y. N.; Gao, W. C.; Lu, X. K. FTIR and simultaneous TG/MS/FTIR study of Late Permian coals from Southern China. *J. Anal. Appl. Pyrolysis* **2013**, *100*, 75−80.

(45) Ma, Y. Y.; Ma, F. Y.; Mo, W. L.; Fan, X. Influence of acid treatment on the structure and extraction performance of Xinjiang Hefeng low-rank coal. *J. Fuel Chem. Technol.* **2019**, *47*, 649−660.

(46) Furmann, A.; Mastalerz, M.; Brassell, S. C.; et al. Extractability of biomarkers from high- and low-vitrinite coals and its effect on the porosity of coal. *Int. J. Coal Geol.* **2013**, *107*, 141−151.

(47) Yan, J. C.; Jiao, H.; Li, Z.; et al. Kinetic analysis and modeling of coal pyrolysis with model-free methods. *Fuel* **2019**, *241*, 382−391.

(48) Liu, P.; Wang, L.; Zhou, Y.; et al. Effect of hydrothermal treatment on the structure and pyrolysis product distribution of Xiaolongtan lignite. *Fuel* **2016**, *164*, 110−118.

(49) Niu, Z.; Liu, G.; Yin, H.; Zhou, C. Devolatilization behaviour and pyrolysis kinetics of coking coal based on the evolution of functional groups. *J. Anal. Appl. Pyrolysis* **2018**, *134*, 351−361.

(50) Luo, R.; Zhou, Q. L. Combustion kinetic behavior of different ash contents coals co-firing with biomass and the interaction analysis. *J. Therm. Anal. Calorim.* **2017**, *128*, 567−580.

(51) Fang, S. W.; Lin, Y.; Huang, Z.; Huang, H. Y.; Chen, S.; Ding, L. X. Investigation of co-pyrolysis characteristics and kinetics of municipal solid waste and paper sludge through TG-FTIR and DAEM. *Thermochim. Acta* **2021**, *700*, No. 178889.

(52) Mo, W. L.; Wu, Z. F.; He, X. Q.; Qiang, W. J.; Wei, B.; Wei, X. Y.; Wu, Y. L.; Fan, X.; Ma, F. Y. Functional group characteristics and pyrolysis/combustion performance of fly ashes from Karamay oily sludge based on FT-IR and TG-DTG analyses. *Fuel* **2021**, *296*, No. 120669.

(53) Fernandez-Lopez, M.; Pedrosa-Castro, G. J.; Valverde, J. L.; Sanchez-Silva, L. Kinetic analysis of manure pyrolysis and combustion processes. *Waste Manage.* **2016**, *58*, 230−240.

(54) He, X. Q.; Mo, W. L.; Wang, Q.; Ma, Y. Y.; Ma, F. Y.; Fan, X.; Wei, X. Y. Effect of swelling treatment by organic solvent on the structure and pyrolysis performance of the direct coal liquefaction residue. *Energy Fuels* **2020**, *34*, 8685−8696.